Synthesis of 2D/2D Structured Mesoporous Co 3 O 4 Nanosheet/N-Doped Reduced Graphene Oxide Composites as a Highly Stable Negative Electrode for Lithium Battery Applications

ARTICLE *in* CHEMISTRY - AN ASIAN JOURNAL · MAY 2015

Impact Factor: 3.94 · DOI: 10.1002/asia.201500466 · Source: PubMed

1 AUTHOR:

Vanchiappan Aravindan

Nanyang Technological University

136 PUBLICATIONS **1,505** CITATIONS

SEE PROFILE

ACES

DOI: 10.1002/asia.201500466

CHEMISTRY
AN ASIAN JOURNAL
Full Paper

Electrochemistry

Synthesis of 2D/2D Structured Mesoporous Co_3O_4 Nanosheet/N-Doped Reduced Graphene Oxide Composites as a Highly Stable Negative Electrode for Lithium Battery Applications

Palanichamy Sennu,[a] Hyo Sang Kim,[a] Jae Youn An,[a] Vanchiappan Aravindan,[b] and Yun-Sung Lee*[a]

Abstract: Mesoporous Co_3O_4 nanosheets (Co_3O_4-NS) and nitrogen-doped reduced graphene oxide (N-rGO) are synthesized by a facile hydrothermal approach, and the N-rGO/Co_3O_4-NS composite is formulated through an infiltration procedure. Eventually, the obtained composites are subjected to various characterization techniques, such as XRD, Raman spectroscopy, surface area analysis, X-ray photoelectron spectroscopy (XPS), and TEM. The lithium-storage properties of N-rGO/Co_3O_4-NS composites are evaluated in a half-cell assembly to ascertain their suitability as a negative electrode for lithium-ion battery applications. The 2D/2D nanostructured mesoporous N-rGO/Co_3O_4-NS composite delivered a reversible capacity of about 1305 and 1501 mAh g^{-1} at a current density of 80 mA g^{-1} for the 1st and 50th cycles, respectively. Furthermore, excellent cyclability, rate capability, and capacity retention characteristics are noted for the N-rGO/Co_3O_4-NS composite. This improved performance is mainly related to the existence of mesoporosity and a sheet-like 2D hierarchical morphology, which translates into extra space for lithium storage and a reduced electron pathway. Also, the presence of N-rGO and carbon shells in Co_3O_4-NS should not be excluded from such exceptional performance, which serves as a reliable conductive channel for electrons and act as synergistically to accommodate volume expansion upon redox reactions. Ex-situ TEM, impedance spectroscopy, and XPS, are also conducted to corroborate the significance of the 2D morphology towards sustained lithium storage.

Introduction

Lithium-ion batteries (LIBs) are attractive energy-storage devices for portable electronic devices that require moderate energy density and low power capability. However, applications such as hybrid electric vehicles (HEVs), electric vehicles (EVs), and grid storage require high-energy-density Li-ion power packs without compromising the power density. To realize the goal of these applications, high-performance materials with low levels of polarization at high current rates are desperately warranted, particularly on the negative side. Along these lines, intense research activity on LIBs is underway. Morphology, crystallinity, and particle size of the materials play a vital role in establishing the performance of such LIBs.[1–6] Li-ion kinetics and electron transport across the electrode/electrolyte interface and electrode surfaces are essential. Furthermore, maintaining the structural stability and reversibility of the electrodes upon repeated redox reactions are also crucial factors.

In a last decade, 2D inorganic nanostructures have turned out to be an important class of materials owing to unique morphologies, intriguing properties, and potential applications. Further, the properties of such 2D materials differing from those of other 0D, 1D, and 3D nanostructures.[7,8] The 2D materials can be employed in hybrid materials that possess numerous applications in heterogeneous catalysis,[9] fuel cells,[10] electrochemical sensing,[11] photoluminescence,[12] and biomolecule/drug reservoirs.[13,14] Recent research activity predominantly focused on the utilization of such fascinating 2D/2D hybrids as high-performance electrode materials for energy-storage applications, preferably LIBs.[15–18] Indeed, the porous nature of 2D nanostructures with a high specific surface area improves electron transport because of highly interconnected particulates. Heteroatomic doping also improves electrode/electrolyte wettability and/or is beneficial for rapid Li-ion kinetics, especially at high current operation.

Materials that undergo conversion (displacement) reactions or alloy formation with metallic Li are considered to be promising solutions for the development of LIBs instead of graphite owing to a high reversible capacity and high power capability. However, alloy-based anodes that experience severe volume expansion and unstable solid–electrolyte interphase (SEI) for-

[a] P. Sennu, H. S. Kim, J. Y. An, Prof. Y.-S. Lee
Faculty of Applied Chemical Engineering
Chonnam National University
Gwang-ju 500-757 (Republic of Korea)
E-mail: leeys@chonnam.ac.kr

[b] Dr. V. Aravindan
Energy Research Institute@NTU (ERI@N)
Nanyang Technological University
Research Techno Plaza, 50 Nanyang Drive, Singapore 637553 (Singapore)

Supporting information for this article is available on the WWW under http://dx.doi.org/10.1002/asia.201500466.

mation prohibit their potential use as anodes in practical cells, although Sony's Nexelion configuration is an exception. Conversion-type anode materials also face similar issues, but to a lesser degree and these can be effectively addressed by various approaches. Since the discovery of conversion reactions in transition-metal oxides by Poizot et al.,[8] several metal oxides have been extensively investigated from the anode point of view. In addition, the same strategy has also been extended to metal sulfides, fluorides, chlorides, and so forth. Of these compounds, Co_3O_4 is appealing in terms of a higher theoretical capacity ($\approx$890 mA h g^{-1} for an 8-electron reaction) and easy synthetic protocol with tailored morphology. However, achieving higher stability and high power capability remains an issue for the aforementioned anode. Thus, an attempt was performed to make the composite with another 2D material, graphene, because it is one of the 2D forms of carbon and possesses unique crystalline properties and excellent electrical conductivity profiles. In addition, the presence of such carbonaceous material overcomes the lack of conductivity issues and upholds the volume variation mentioned earlier. So, the high power capability of Co_3O_4 can be easily achieved. To further extend the electrochemical activity for improved Li-storage, heteroatom (N, S, and B) doping at the interfaces and surfaces of the porous structure of the graphene layer has been used to augment the nanoscale reactivity and electrical conductivity.[19] Herein, hierarchical mesoporous Co_3O_4 nanosheets (Co_3O_4-NS) and nitrogen-doped reduced graphene oxide (N-rGO) were synthesized by using a facile hydrothermal method. Then, a 2D/2D structured hierarchical mesoporous N-rGO/Co_3O_4-NS composite was prepared by an infiltration process. Extensive structural and electrochemical properties were evaluated for N-rGO/Co_3O_4-NS composite and described in detail. In addition, ex-situ studies like TEM and XPS were also conducted to reveal the reaction mechanism of Co_3O_4 with Li.

Results and Discussion

Figure 1 presents the XRD patterns of as-prepared hierarchical mesoporous Co_3O_4-NS, GO, N-rGO, and mesoporous N-rGO/Co_3O_4-NS composite. The formation of phase-pure structures for both Co_3O_4-NS and N-rGO/Co_3O_4-NS is clear. The sharp reflections are indicative of the highly crystalline nature of the synthesized product and indexed according to the cubic spinel structure of Co_3O_4 with the *Fd*3*m* space group, which is consistent with that reported in the literature (ICSD 98-002-4210). The average crystallite size value of the mesoporous nanosheets is calculated to be about 20 nm by using the Scherrer formula (calculated based on the predominant reflection at 36.8°). In addition, the XRD pattern of N-rGO clearly revealed the presence of a broad reflection at $2\theta \approx 24.1°$, which corresponded to the (002) crystal plane of disordered carbon with a highly stacked structure (Figure 1, inset). However, in the N-rGO/Co_3O_4-NS composite, there are no distinct reflections observed between $2\theta \approx 23$ and 27° compared with those of Co_3O_4-NS. This clearly indicates that the N-rGO sheets are homogeneously distributed throughout Co_3O_4-NS and no significant aggregation occurs during infiltration. In other words, the

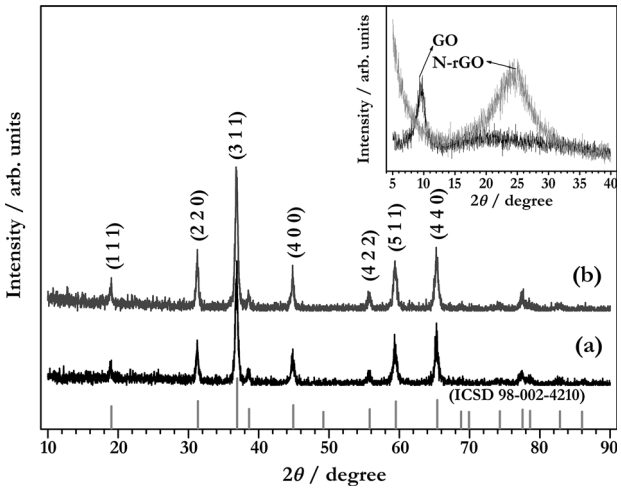

Figure 1. XRD patterns of a) pristine Co_3O_4-NS and b) the N-rGO/Co_3O_4-NS composites. The patterns for GO and N-rGO are given in the inset.

amount of N-rGO in the composite is too low to be detected with the limitations of the X-ray diffractometer. Although Co_3O_4-NS is considered to be a pure-phase material, it contains a negligible amount of residual carbon ($\approx$0.46 wt%) derived from the polymer PVP added during the synthesis. Similarly, N-rGO/Co_3O_4-NS also contains a similar amount of residual carbon, excluding graphene (Figure S1 in the Supporting Information).

Raman spectroscopy is a versatile technique to provide useful information about the functional groups and crystalline nature of the mesoporous N-rGO/Co_3O_4-NS composites, particularly carbonaceous materials. Figure 2 shows the Raman spectra of bare and N-rGO-infiltrated Co_3O_4-NS. Five characteristic bands between $\tilde{\nu} \approx 190$ and 750 cm^{-1} are observed; these are associated with different vibrational modes of crystalline Co_3O_4 (e.g., species with the tetrahedral (Td) symmetry of CoO_4, F2 g(1) and F2 g(2) species with weak symmetry, and Ag(1) species with octahedral (Oh) symmetry of CoO_6).[22,23] The bands located at $\tilde{\nu} \approx 1360$ and 1600 cm^{-1} in the N-rGO/Co_3O_4-NS composite correspond to characteristic D and G bands of car-

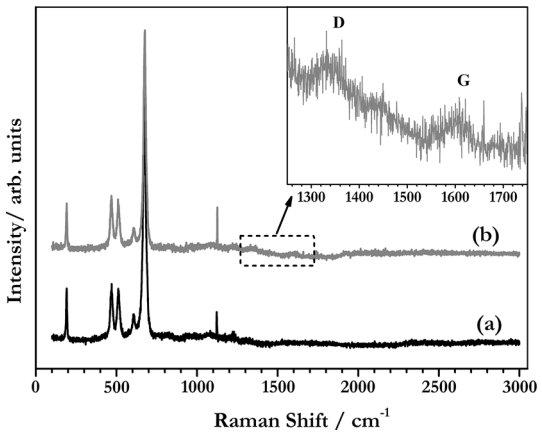

Figure 2. Raman spectra of a) pristine Co_3O_4-NS and b) the N-rGO/Co_3O_4-NS composites. The inset indicates the characteristic D and G bands of rGO.

bonaceous materials, namely, graphene (Figure 2, inset, and Figure S2 in the Supporting Information).[24] This further confirms the presence of graphene nanosheets in the composites.

The porosity and specific surface area of the composite and pristine materials were investigated by nitrogen adsorption/desorption studies (Figure 3). BET specific surface areas of 99.7

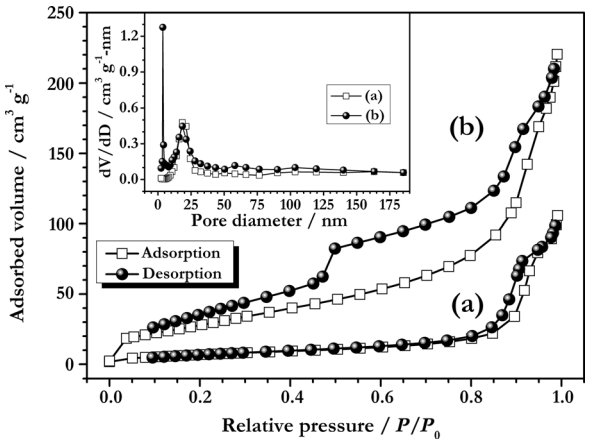

Figure 3. Nitrogen adsorption/desorption isotherms for a) pristine Co_3O_4-NS and b) the N-rGO/Co_3O_4-NS composite. The inset shows characteristic Barrett–Joyner–Halenda (BJH) pore size distributions.

and 27.2 $m^2 g^{-1}$ are noted for the N-rGO/Co_3O_4-NS composite and Co_3O_4-NS, respectively. The presence of a high surface area is mainly because of the presence of graphene nanosheets. The hysteresis loop at a high relative pressure indicates the presence of mesoporosity with a type IV isotherm. It can be seen from the BJH distribution that the composites have two types of pores (3.77 and 18.3 nm), whereas a single distribution at 18.51 nm only is noted for the Co_3O_4-NS (Figure 3, inset). The BET specific surface areas, pore diameters, total pore volumes, and pore sizes of the mesoporous N-rGO/Co_3O_4-NS composite and pristine material are listed in Table 1. High specific surface areas with different pore sizes can accommodate more electrolyte solutions, which translate into better electrochemical profiles and are also expected to sustain volume changes upon the charge–discharge process.

The FE-SEM images clearly showed the uniformity and crystal regularity of the mesoporous N-rGO/Co_3O_4-NS composite and pristine Co_3O_4-NS (Figure 4). It is clear that pristine Co_3O_4 consists of a 2D sheet-like morphology of nearly perfect rectangles with dimensions of 4 to 8 μm and thicknesses of 70–90 nm (Figure 4b, inset). The magnified view clearly demonstrates the selective and specific assembly of uniform nanoparticles in pristine Co_3O_4-NS. On the other hand, in the N-rGO/Co_3O_4-NS composite, there is no deviation in the morphology noted, but N-rGO sheets are anchored parallel to the Co_3O_4-NS surface to form an ordered layered-like structure (Figure 4d, inset). This 2D/2D assembly gives rise to good interlinking of individual sheets and better interfacial contact than other-dimensional composites (1D/2D, 2D/3D). This clearly reveals that uniform conventional mesopores with widespread network morphology were produced by our preparation method.

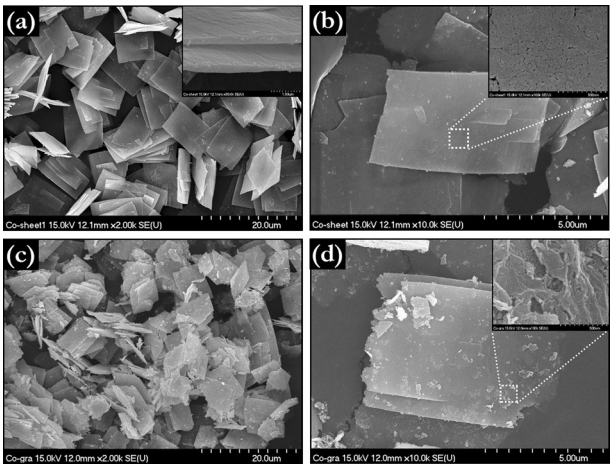

Figure 4. Low- and high-magnification FE-SEM images of pristine Co_3O_4-NS (a and b) and N-rGO/Co_3O_4-NS composites (c and d). The inset in b) shows the porous nature of pristine Co_3O_4-NS, and the inset in d) confirms the 2D/2D attachment of a graphene shell to Co_3O_4-NS.

The microscopic structure of the mesoporous N-rGO/Co_3O_4-NS composite was characterized by TEM studies (Figure 5). Figure 5 shows that the N-rGO/Co_3O_4-NS composites maintain their 2D structure without noticeable changes during the infiltration process; this is consistent with FE-SEM observations. The attachment of transparent N-rGO sheets (Figure S3a and d in the Supporting Information) on Co_3O_4-NS could be confirmed from analysis of the edge, such as that shown in Figure 5a, which indicates intimate contact and integration between N-rGO and Co_3O_4-NS. The nanosheets are composed of numerous, randomly oriented 17–25 nm sized nanoparticles with conventional mesopores in the matrix (Figure 5b, inset, and Figure S3b in the Supporting Information). The observed sizes are consistent with BJH pore size distributions. The HR-TEM image in Figure 5c shows that the primary core of Co_3O_4-NSs is well coated and connected with a carbon-shell-like core–shell morphology with the hierarchical growth of thin nanosheets. The measured lattice spacings of 0.245, 0.278, and 0.435 nm correspond to interlayer spacings of the (113),

Table 1. BET surface areas, total pore volumes, and pore sizes of hierarchical mesoporous Co_3O_4-NS and mesoporous N-rGO/Co_3O_4-NS composites.

Sample	S_{BET}[a] [$m^2 g^{-1}$]	V_{total}[b] [$cm^3 g^{-1}$]	Pore size[c] [nm]	Average pore diameter [nm]	N-rGO content [wt%]
Co_3O_4-NS	27.153	0.1579	18.51	23.258	0
N-rGO/Co_3O_4-NS	99.743	0.3378	3.77 and 18.51	13.548	10

[a] S_{BET} is the BET surface area. [b] The total pore volume (V_{total}) was the single-point adsorption total pore volume of pores less than 400 nm in diameter at $P/P_0 = 0.990$. [c] The pore size is the BJH adsorption average pore diameter.

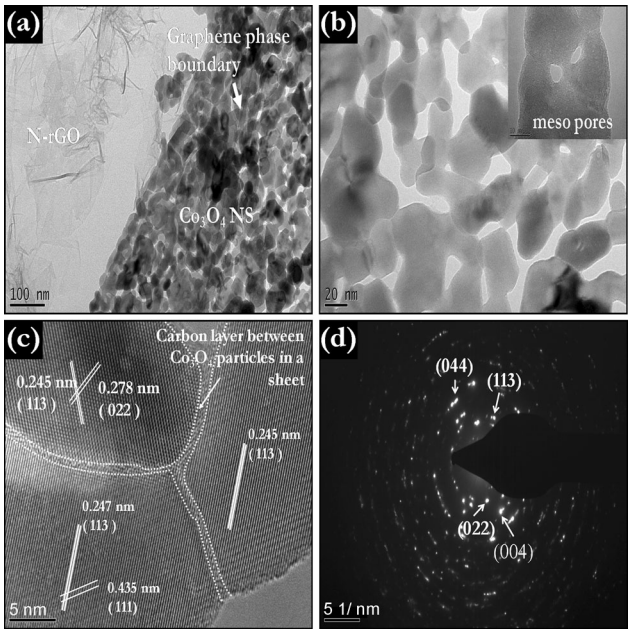

Figure 5. a) and b) TEM images of the 2D/2D layered mesoporous structure of N-rGO/Co_3O_4-NS composites, c) high-resolution (HR) TEM image of the crystalline core–shell structure, and d) the selected-area electron diffraction (SAED) pattern.

(022), and (111) crystal planes, respectively. The formation of single-crystalline particulates is also confirmed. However, in the SAED pattern, polycrystalline-like features are observed. This is because of overlap of the particulates during recording of the SAED pattern and confirms the cubic spinel phase of Co_3O_4.

The surface chemical composition of the N-rGO/Co_3O_4-NS composite is confirmed by XPS studies (Figure 6). Figure 6a shows the survey spectrum of the N-rGO/Co_3O_4-NS composite, which is composed of cobalt, carbon, nitrogen, and oxygen. The Co 2p core level spectrum contains two main peaks associated with the Co $2p_{3/2}$ and Co $2p_{1/2}$ levels and can be further deconvoluted into four sublevels (Figure 6b). The two peaks at 781.8 and 796.6 eV are assigned to the Co^{2+} state, whereas two other peaks positioned at 779.5 and 794.5 eV are attributed to the existence of Co^{3+} ions.[25–27] The spin–orbit splitting is about 14.7 eV which clearly suggest the formation of Co_3O_4. The deconvoluted C 1s spectrum showed four additional sublevels (Figure 6c). The C 1s peaks clearly exhibits a considerable degree of oxidation with four components corresponding to various functionalities over carbonaceous materials; these include non-oxygenated ring C=C bonding at 284.6 eV, C–O bonding at 286.03 eV, the carbonyl carbon (C=O) at 287.3 eV, and the carboxylate carbon (O–C=O) at 288.4 eV. This clearly indicates the presence of surface functional groups over carbonaceous materials. Furthermore, we also verified nitrogen doping in rGO sheets during the hydrothermal reaction, which is clearly supported from the core-level N 1s spectra (Figure S4 in the Supporting Information).[28,29]

The electrochemical performances of the N-rGO/Co_3O_4-NS composite and pristine Co_3O_4-NS were evaluated in a half-cell assembly (vs. Li) in both potentiostatic and galvanostatic modes. Cyclic voltammograms were recorded between 0.01 and 3.0 V vs. Li at a slow scan rate of 0.1 mV s^{-1} (Figure 7). In the first cathodic scan, a small peak at around 1.06 V vs. Li was noted because of irreversible Li insertion into the spinel phase ($Li_xCo_3O_4$). During the continuous discharge process, very prominent ($\approx$0.86 V vs. Li) and weak potentials ($\approx$0.7 vs. Li) are observed, which correspond to the destruction of the crystal structure and decomposition of the electrolyte solution. The decomposition of the electrolyte solution eventually leads to the formation of the SEI over the electroactive material, which is composed of polymeric films, inorganic byproducts, and so forth. The overall reaction in the first discharge process can be described by Equation (1).

$$Co_3O_4 + x\,Li^+ + x\,e^- \rightarrow Li_xCo_3O_4 \rightarrow 3\,Co^0 + 4\,Li_2O \quad (1)$$

During the subsequent anodic scan, a broad peak located at about 2.13 V vs. Li is ascribed to the re-oxidization of metallic cobalt and the decomposition of Li_2O according to the reversible conversion mechanism described by Equation (2).[30–32]

$$3\,Co + 3\,Li_2O \leftrightarrow Co_3O_4 \quad (2)$$

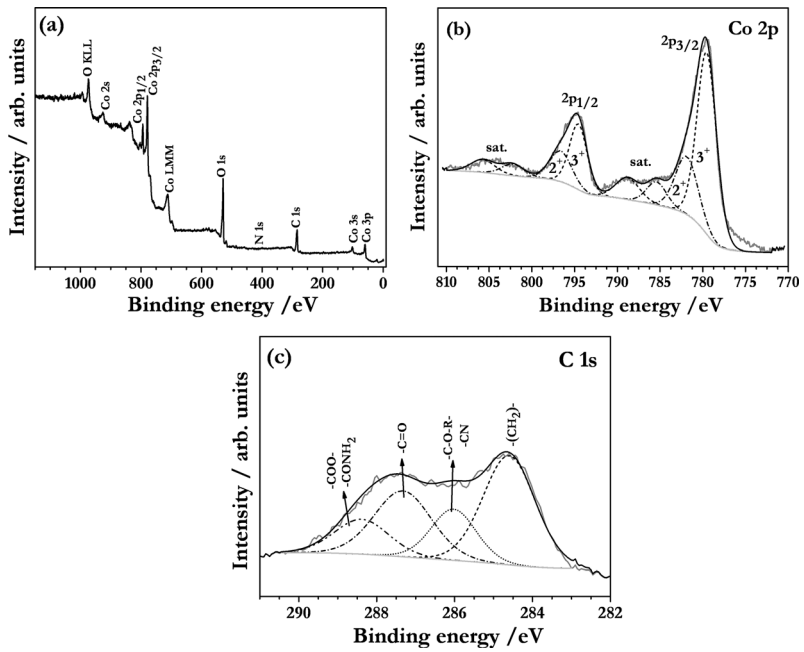

Figure 6. XPS spectra of the N-rGO/Co_3O_4-NS composite: a) survey, b) Co 2p, and c) carbon spectra.

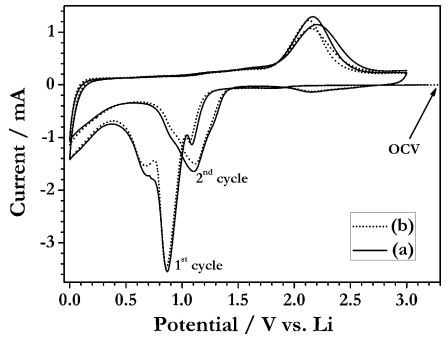

Figure 7. Comparative cyclic voltammograms of a) pristine Co_3O_4-NS and b) the N-rGO/Co_3O_4-NS composite collected at a slow scan rate of 0.1 mV s^{-1} between 0.01 and 3.0 V vs. Li at room temperature.

In the subsequent cycle, shifting of the peak potential towards a higher potential (≈0.86 to ≈1.11 V vs. Li) is noted to be accompanied by an apparent decrease in the area underneath the curve. On the other hand, a negligible shift in the peak positions is noted for the anodic scan (≈2.13 to ≈2.14 V vs. Li). It is worth mentioning that the two electrodes follow similar trends with no noticeable difference between them. The observed peak shift and concomitant current decrease might signify the formation of a thick SEI layer and graphene layers in the composite might also impede ion transport.[33,34] To validate the reaction mechanism described above, we conducted ex situ HR-TEM studies for the N-rGO/Co_3O_4-NS composite electrode (Figure 8). The HR-TEM image was recorded in the charged state (i.e., 3 V vs. Li) after the completion of 50 cycles. No significant aggregation occurred during cycling (Figure S3c in the Supporting Information), and the core–shell structure persisted with proper electrical conduction as well. From the SAED pattern, the measured lattice spacings are 0.247 and 0.281 nm, which correspond to the (113) and (022) crystal planes, respectively, of cubic spinel Co_3O_4. This is clearly revealed from the appearance of bright rings (Figure 8b, inset). TEM analysis clearly suggests the dimensionality and integrity of the N-rGO/Co_3O_4-NS composite upon cycling, and has a significant influence on the conversion reactions and interfacial and surface Li storage. XPS studies were also conducted to ensure the re-formation of Co_3O_4 upon the charging process and the survey spectrum of the cycled electrode is given in Figure 8c. The binding energies of the two major peaks, Co $2p_{3/2}$ and Co $2p_{1/2}$, are located in the ranges of 781–784 and 795.7–798.5 eV, respectively.[26,27,35] The strong shakeup satellite peaks located at 790.5 and 806 eV shifted to higher binding-energy levels by about 2 eV relative to the as-prepared composite. The intensity ratio of both peaks decreased about sixfold, with the satellite peak occurring at binding energies 3–9 eV higher than those of the main peak. Therefore, based on the peak widths and positions of the satellites apart from the main peaks, spin–orbital splitting of Co $2p_{3/2}$ and Co $2p_{1/2}$ is about 15 eV. Comparatively, both signals could be attributed to a typical Co_3O_4 phase with the mixed-valence state of Co^{2+} and Co^{3+} (Figure 8d). The XPS study also clearly confirmed the re-formation of Co_3O_4 upon charging from the metallic (Co^0) state and agreed well with ex situ TEM analysis.

Li-ion transport kinetics were studied by using electrochemical impedance spectroscopy (EIS) in the two-electrode coin-cell geometry (Figure 9). The Nyquist plots for N-rGO/Co_3O_4-NS and pristine Co_3O_4-NS electrodes before and after cycling consist of three main regimes. The depressed semicircles in the high-frequency regions are associated with the electrolyte resistance (R_s) and the high–middle frequency region is assigned to contact and charge-transfer resistance across the electrode/electrolyte interface (R_{ct}). Finally, the vertical tail inclined at 45° in the low-frequency region, as one would expect for capacitance behavior (Warburg element). The R_s and R_{ct} values for N-rGO/Co_3O_4-NS and pristine Co_3O_4-NS are 5.5/36 and 5.3/34 Ω, respectively. After cycling of the spinel-phase electrodes, the R_{ct} values decreased dramatically from 36 to 12 Ω for N-rGO/Co_3O_4-NS and 34 to 14 Ω for pristine Co_3O_4-NS. This striking phenomenon is in good agreement with previous reports.[36,37] During cycling, the R_{ct} resistance decreased substantially for Co_3O_4-NS, which may be related to stabilization of the SEI layer and activation of the core–shell carbon materials. The hierarchical mesoporous structure in Co_3O_4-NS can accommodate more

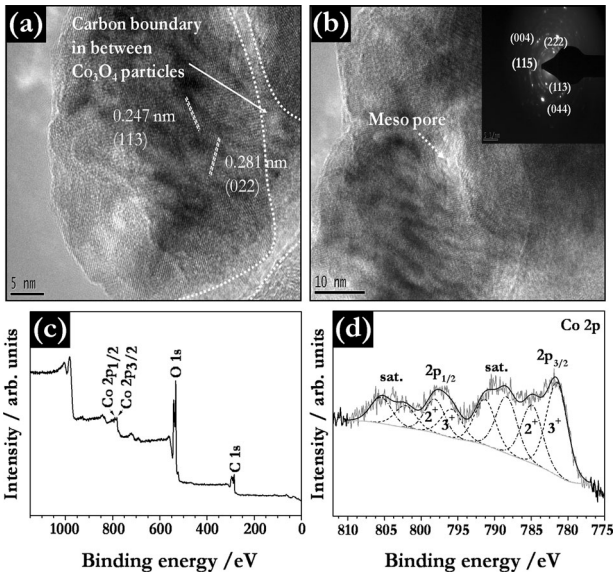

Figure 8. The N-rGO/Co_3O_4-NS composite electrodes after cycling: a) HR-TEM image of the crystalline core–shell structure, and b) SAED pattern. XPS c) survey and d) Co 2p spectra.

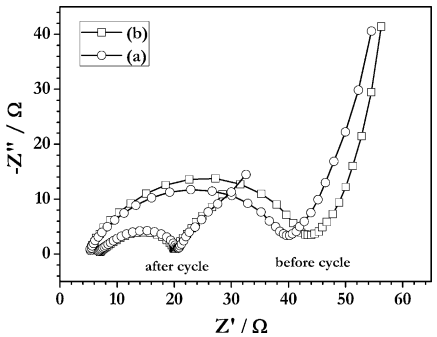

Figure 9. Comparative Nyquist plots collected before and after cycling of a) pristine Co_3O_4-NS and b) the N-rGO/Co_3O_4-NS composite.

electrolytes (allowing facile electrolyte pathways), which may facilitate interfacial charge transfer at the nanoscale level in the electrode/electrolyte interface. The noticeable reduction in R_{ct} after the fifth cycles in both cases suggests that, with the increase in cycling, electrolyte wetting through the mesopores gradually increases and eventually translates into a beneficial effect on the stabilization of the SEI layer (Figure S5 in the Supporting Information). In comparison with Co_3O_4-NS, the low-frequency region pertaining to the capacitive behavior is still more prominent and substantiates the above claim.

Then, we investigated the Li-storage properties of the mesoporous N-rGO/Co_3O_4-NS composite and pristine Co_3O_4-NS in the half-cell assembly in galvanostatic mode under constant current densities of 80 and 1000 mA g^{-1}. Figure 10 shows typical galvanostatic charge/discharge curves in the 0.01–3.0 V vs. Li region. A prominent short plateau observed at around 1.2 V vs. Li corresponds to Li insertion into the Co_3O_4 phase and is found at around 1.67 ($Li_{1.67}Co_3O_4$) and 1.98 mol ($Li_{1.98}Co_3O_4$) of Li for pristine and N-rGO infiltrated Co_3O_4-NS, respectively. Seemingly, the amount of Li intake decreases upon increasing the current rate from 80 to 1000 mA g^{-1}. Eventually, the presence of two long voltage plateaus at around 1.06 and 0.87 V vs. Li in the early discharge profiles are associated with conversion reactions and electrolyte decomposition. The observed reactions are completely corroborated by the cyclic voltammetry measurements described above (Figure S6 in the Supporting Information). Initial discharge capacities of about 2638 and 1191 mAh g^{-1} are observed for the N-rGO/Co_3O_4-NS composite and about 2035 and 1124 mAh g^{-1} for pristine Co_3O_4-NS at current densities of 80 and 1000 mA g^{-1}, respectively. The irreversible capacity loss in the first cycle is mainly attributed to the formation of SEI layer, which consumes more Li in an irreversible manner.[38] The shapes of the profiles were not significantly altered upon cycling, which indicates the excellent stability and integrity of the 2D structure of Co_3O_4; for instance, the shape of the 50th discharge cycle profile is similar to that of the second cycle (Figure S7 in the Supporting Information). However, a shift in the peak towards lower potential and marginal increase in Li uptake in the intercalation process is worth mentioning. Reversible capacity areas as high as about 1523 and 815 mAh g^{-1} for the N-rGO/Co_3O_4-NS composite and about 1327 and 790 mAh g^{-1} for pristine Co_3O_4-NS at 80 and 1000 mA g^{-1}, respectively, are observed. The observed capacity profiles for both pristine and N-rGO/Co_3O_4-NS are much higher than the theoretical capacity and can be calculated from Equation (3),[39,40]

$$C_{theoretical} = C_{Co_3O_4}[Co_3O_4]\ (\text{in wt}\%) + C_{carbon}[C]\ (\text{in wt}\%) = 875.4\ \text{mAh g}^{-1}, \quad (3)$$

in which $C_{Co_3O_4} \approx 890$ mAh g^{-1} and $C_{carbon} \approx 744$ mAh g^{-1} (because graphene involves the Li adsorption/desorption on both sides of the sheets, which results in twice the theoretical capacity of graphite). The excess reversible capacity is mainly attributed to non-Faradaic Li storage, called pseudocapacitance, which is an interfacial reaction owing to charge separation across the metal/Li_2O phase boundary.[41,42] The presence of mesopores in Co_3O_4 greatly enhances interfacial and surface Li storage, which provides short path lengths with less resistance for electron transport at the electrode/electrolyte interface. Thus, the enhanced electrochemical profiles result. The formation of a surface polymeric layer, which is a main component of the SEI, is beneficial in terms of preserving the 2D structure upon prolonged cycling, although it consumes more Li in the initial cycles.[22]

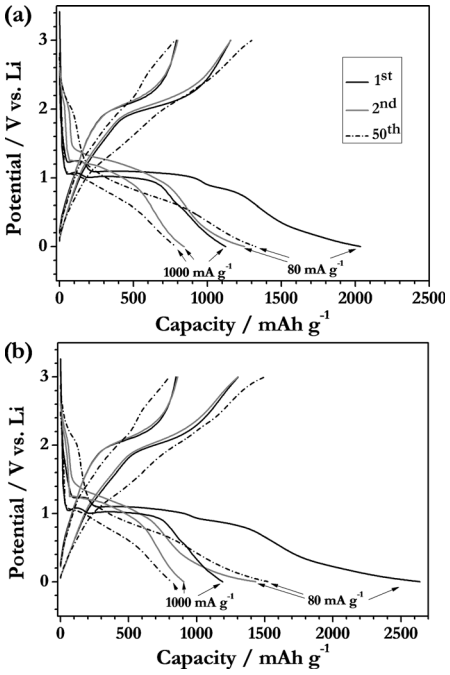

Figure 10. Galvanostatic 1st, 2nd, and 50th cycle charge/discharge profiles for a) pristine Co_3O_4-NS and b) N-rGO/Co_3O_4-NS composite at current densities of 80 and 1000 mA g^{-1}.

Figure 11 displays the cycling performance of hierarchical mesoporous N-rGO/Co_3O_4-NS and pristine Co_3O_4-NS in the half-cell assembly at various current densities. Reversible capacities in the second cycle (and Columbic efficiency) of about 1433 ($\approx$91%) and 906 mAh g^{-1} ($\approx$95%) are noted for the N-rGO/Co_3O_4-NS composite, and about 1250 ($\approx$93%) and 842 mAh g^{-1} ($\approx$95%) for pristine Co_3O_4-NS at current rates of 80 and 1000 mA g^{-1}, respectively. It is worth noting that the gradual increase in capacity from the second cycle is the result of gradual activation of interconnected core–shell materials and consistent with previous reports in the literature.[7,41,43,44] In addition, the long-term cyclability was also measured at a current density of 1 A g^{-1}, for which reversible capacities of about 543 and 426 mAh g^{-1} are noted after 200 cycles for the N-rGO/Co_3O_4-NS composite and Co_3O_4-NS, respectively (Figure S9 in the Supporting Information). Even after 200 cycles at a high current rate, the reversible capacity is still higher than the theoretical limitations of conventional graphite; the 2D/2D nanostructures also improve the electrochemical properties like interfacial and surface Li storage, apart from the classical conversion reaction. Also, the carbon coating on the Co_3O_4 core–shell nanoparticles maintains the electrical conduction pathway, acts as a buffer matrix to prevent particle agglomeration, and maintains structural stability during the discharging/

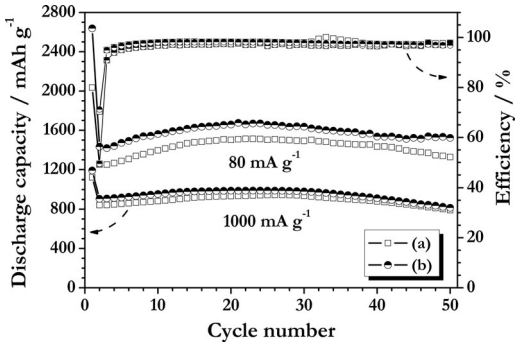

Figure 11. Cycling performance comparison of a) pristine Co_3O_4-NS and b) the N-rGO/Co_3O_4-NS composite at current densities of 80 and 1000 mA g^{-1}.

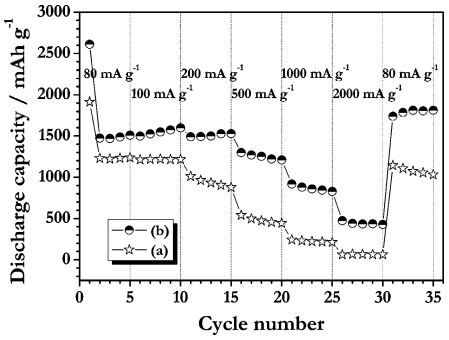

Figure 12. Comparative rate capability of a) pristine Co_3O_4-NS and b) the N-rGO/Co_3O_4-NS composite at different current densities.

charging process, which is not neglected for improved electrochemical activity. Based on the above results, the outstanding high current performance of hierarchical mesoporous Co_3O_4-NS and composites with graphene are the best values of various Co_3O_4 nanostructures reported, irrespective of the morphology.[40,45–49] Furthermore, we strongly believe that the high capacity and rate capability are undoubtedly derived from their unique hierarchical mesoporous morphology.

Generally, good rate performance of the electrode materials is desirable for the fabrication of high-power and high-energy Li-ion power packs. We evaluated the rate capability of the N-rGO/Co_3O_4-NS composite and pristine Co_3O_4-NS as electrodes at different current densities (from 80 to 2000 mA g^{-1}; Figure 12). The N-rGO/Co_3O_4-NS composite exhibits a better rate capability, especially at high current rates, than that of pristine Co_3O_4-NS, with average discharge capacities of about 1488, 1525, 1500, 1254, 859, and 434 mAh g^{-1} at current densities of 80, 100, 200, 500, 1000, and 2000 mA g^{-1}, respectively. It can be clearly seen that, even at current densities as high as 2000 mA g^{-1}, about 367 mAh g^{-1} of the capacity is retained, which is comparable to that of commercially available graphite. More importantly, when the current density was scanned back to 80 mA g^{-1}, a discharge capacity of about 1713 mAh g^{-1} was noted, which indicated the good reversibility of the material. From this point of view, the excellent rate capabilities of these materials demonstrate that mesopores with conductive channels are beneficial for fast redox reactions with improved kinetics. Nanoscopic subunits are activated during cycling, which is an important factor, that is, Li-ion and electron diffusion to/from the electrolyte/particle interface, and these materials have great potential as high-rate anode materials in LIBs.

Conclusion

We successfully synthesized a hierarchical mesoporous Co_3O_4-NS and N-rGO from a facile hydrothermal method. The mesoporous N-rGO/Co_3O_4-NS composite was prepared through an infiltration process and delivered high reversible capacities of about 1501 and 800 mA h g^{-1} after 50 cycles at current densities of 80 and 1000 mA g^{-1}, respectively. The hierarchical mesoporous network provided extra space for Li storage and reduced the electron diffusion length. The presence of mesoporosity enhanced the electrode/electrolyte contact and provided extra active sites for the redox reaction and more interfacial bonding sites. The N-rGO material not only accommodated volumetric strain observed during the electrochemical reaction, but also served as an excellent conductive matrix in the 2D/2D composite. As a result, the unique features of hierarchical mesoporous N-rGO/Co_3O_4-NS, such as high capacity, good cyclability, and high rate capability, result in it being a promising anode material for the construction of next-generation high-power Li-ion power packs. The same concept can be extended to other metal oxides to realize high-energy and high-power capabilities.

Experimental Section

Synthesis of Co_3O_4-NS, N-rGO, and N-rGO/Co_3O_4-NS Composites

A conventional hydrothermal route was employed to prepare the large-area hierarchical mesoporous Co_3O_4-NS in a simple and cost-effective manner. In a typical process, $CoCl_2{\cdot}6H_2O$ (1 g; Wako, Japan) and urea (4 g; Junsei, Japan) were dissolved in distilled water (70 mL) by intense stirring for 10 min. Then, polyvinylpyrrolidone (PVP; 1 g; $M_W = 40\,000$, Sigma–Aldrich, USA) was added as a surfactant to the transparent pink solution, which was then stirred for 1 h at room temperature. The resulting suspension was transferred to a Teflon-lined stainless-steel autoclave and heated to 120 °C for 24 h. The precipitate was filtered and washed with water and ethanol several times. Finally, the products were calcined at 400 °C for 3 h in a tube furnace to yield the desired Co_3O_4-NS.

First, graphene oxide (GO) was synthesized from graphite flakes by a well-known modified Hummers method.[20] GO suspensions were obtained from the as-synthesized mixtures of GO/H_2O (3 mg mL^{-1}) from probe sonication for 30 min (Vibra-Cell, Sonic, USA). Chemical reduction of the solution of GO (350 mL) to form N-rGO was achieved by adding ammonia (to pH 10) and hydrazine hydrate (30 mL; 64–65 %, Sigma–Aldrich, USA) as reducing agents under hydrothermal conditions, as described elsewhere.[21] The solution was then transferred into a Teflon-lined autoclave and heated to 180 °C for 6 h. The N-rGO sheets were collected by means of centrifugation and washed with deionized water and ethanol several times. Finally, the collected samples were dried at 60 °C for 12 h.

The mesoporous N-rGO/Co_3O_4 NS composites were prepared by an infiltration method. N-rGO was well dispersed in ethanol

(1 mg mL^{-1}) by sonication, and then Co_3O_4-NS were added in the desired weight ratio (10:90%) to the solution of N-rGO. Mutual electrostatic interactions between functionalized graphene and Co_3O_4-NS resulted in the anchoring of metal oxide particle over N-rGO sheets. The final N-rGO/Co_3O_4-NS composite was obtained by vacuum filtration of the above mixed solution.

Electrode Preparation and Characterization

Powder XRD patterns of the composite and pristine materials were recorded by using a Rint 1000 diffractometer (Rigaku, Japan) equipped with $Cu_{K\alpha}$ radiation. Raman spectra of the composite materials were recorded by using a Lab Ram HR 800 Raman dispersive spectrometer (Horiba, Japan). The BET specific surface area of the samples was analyzed by using an ASAP 2010 surface analyzer (Micromeritics, USA). Surface morphological features and the internal structure of the materials were examined by field-emission (FE) SEM (S-4700, Hitachi, Japan) and TEM (TecnaiF20, Philips, the Netherlands). X-ray photoelectron spectroscopy (XPS) was performed by using a Multicar 2000 (UK) instrument. Electrochemical studies were carried out by using an SP-150 electrochemical analyzer (Bio-Logic, France).

All electrochemical measurements were performed by using a CR2032 coin cell configuration. The composite and pristine electrodes were formulated by pressing the slurry (72% active materials, 14% Ketjen black (KB), and 14% Teflonized acetylene black (TAB)) into a 200 mm^2 stainless-steel mesh current collector followed by drying at 160 °C for 4 h in a vacuum oven. The test cells were fabricated in an argon-filled glove box with metallic Li as a counter electrode, which was separated by a Celgard 3401 membrane, and filled with 1 M $LiPF_6$ in ethylene carbonate (EC)/dimethyl carbonate (DMC; 1:1 v/v, Soulbrain Co., Ltd, Korea) electrolyte. The charge–discharge characteristics of the cells were evaluated (0.01–3 V vs. Li) at different current densities at room temperature.

Acknowledgements

This work was supported by the International Cooperation of the Korea Institute of Energy Technology Evaluation and Planning (KETEP) grant funded by the Korean Government Ministry of Knowledge Economy (no. 20128510010050).

Keywords: cobalt · electrochemistry · lithium-ion batteries · mesoporous materials · nanostructures

[1] M. G. Kim, J. Cho, *Adv. Funct. Mater.* **2009**, *19*, 1497.
[2] J. L. Gunjakar, I. Y. Kim, J. M. Lee, Y. K. Jo, S.-J. Hwang, *J. Phys. Chem. C* **2014**, *118*, 3847.
[3] V. Aravindan, J. Gnanaraj, Y.-S. Lee, S. Madhavi, *Chem. Rev.* **2014**, *114*, 11619.
[4] V. Aravindan, J. Gnanaraj, Y.-S. Lee, S. Madhavi, *J. Mater. Chem. A* **2013**, *1*, 3518.
[5] V. Aravindan, Y.-S. Lee, R. Yazami, S. Madhavi, *Mater. Today,* **2015**, *6*, 345.
[6] V. Aravindan, Y. S. Lee, S. Madhavi, *Adv. Energy Mater.* **2015**, DOI: 10.1002/aenm.201402225.
[7] K. M. Shaju, F. Jiao, A. Debart, P. G. Bruce, *Phys. Chem. Chem. Phys.* **2007**, *9*, 1837.
[8] P. Poizot, S. Laruelle, S. Grugeon, L. Dupont, J. M. Tarascon, *Nature* **2000**, *407*, 496.
[9] J. L. Gunjakar, T. W. Kim, H. N. Kim, I. Y. Kim, S.-J. Hwang, *J. Am. Chem. Soc.* **2011**, *133*, 14998.
[10] S. I. Shin, A. Go, I. Y. Kim, J. M. Lee, Y. Lee, S.-J. Hwang, *Energy Environ. Sci.* **2013**, *6*, 608.
[11] S. Wu, Z. Zeng, Q. He, Z. Wang, S. J. Wang, Y. Du, Z. Yin, X. Sun, W. Chen, H. Zhang, *Small* **2012**, *8*, 2264.
[12] S. Ida, C. Ogata, U. Unal, K. Izawa, T. Inoue, O. Altuntasoglu, Y. Matsumoto, *J. Am. Chem. Soc.* **2007**, *129*, 8956.
[13] D.-H. Park, J.-H. Choy, *Eur. J. Inorg. Chem.* **2012**, 5145.
[14] J.-M. Oh, D.-H. Park, J.-H. Choy, *Chem. Soc. Rev.* **2011**, *40*, 583.
[15] S. Y. Han, I. Y. Kim, S.-H. Lee, S.-J. Hwang, *Electrochim. Acta* **2012**, *74*, 59.
[16] K. M. Lee, Y. R. Lee, I. Y. Kim, T. W. Kim, S. Y. Han, S.-J. Hwang, *J. Phys. Chem. C* **2012**, *116*, 3311.
[17] Y. R. Lee, I. Y. Kim, T. W. Kim, J. M. Lee, S.-J. Hwang, *Chem. Eur. J.* **2012**, *18*, 2263.
[18] T. W. Kim, T. S. Jung, S.-H. Hyun, S.-J. Hwang, *Mater. Lett.* **2010**, *64*, 565.
[19] Z.-S. Wu, W. Ren, L. Xu, F. Li, H.-M. Cheng, *ACS Nano* **2011**, *5*, 5463.
[20] D. C. Marcano, D. V. Kosynkin, J. M. Berlin, A. Sinitskii, Z. Sun, A. Slesarev, L. B. Alemany, W. Lu, J. M. Tour, *ACS Nano* **2010**, *4*, 4806.
[21] D. Long, W. Li, L. Ling, J. Miyawaki, I. Mochida, S.-H. Yoon, *Langmuir* **2010**, *26*, 16096.
[22] L. Y. Pan, H. B. Zhao, W. C. Shen, X. W. Dong, J. Q. Xu, *J. Mater. Chem. A* **2013**, *1*, 7159.
[23] A. C. Ferrari, J. Robertson, *Phys. Rev. B* **2000**, *61*, 14095.
[24] F. Tuinstra, J. L. Koenig, *J. Chem. Phys.* **1970**, *53*, 1126.
[25] B. Varghese, C. H. Teo, Y. Zhu, M. V. Reddy, B. V. R. Chowdari, A. T. S. Wee, V. B. C. Tan, C. T. Lim, C. H. Sow, *Adv. Funct. Mater.* **2007**, *17*, 1932.
[26] T. J. Chuang, C. R. Brundle, D. W. Rice, *Surf. Sci.* **1976**, *59*, 413.
[27] K. Hirokawa, F. Honda, M. Oku, *J. Electron Spectrosc. Relat. Phenom.* **1975**, *6*, 333.
[28] J. W. Lee, A. S. Hall, J.-D. Kim, T. E. Mallouk, *Chem. Mater.* **2012**, *24*, 1158.
[29] R. Gokhale, V. Aravindan, P. Yadav, S. Jain, D. Phase, S. Madhavi, S. Ogale, *Carbon* **2014**, *80*, 462.
[30] D. Larcher, G. Sudant, J. B. Leriche, Y. Chabre, J. M. Tarascon, *J. Electrochem. Soc.* **2002**, *149*, A234.
[31] B. Zhang, Y. B. Zhang, Z. Z. Miao, T. X. Wu, Z. D. Zhang, X. G. Yang, *J. Power Sources* **2014**, *248*, 289.
[32] G. L. Wang, J. C. Liu, S. Tang, H. Y. Li, D. X. Cao, *J. Solid State Electrochem.* **2011**, *15*, 2587.
[33] F. Wang, C. C. Lu, Y. F. Qin, C. C. Liang, M. S. Zhao, S. C. Yang, Z. B. Sun, X. P. Song, *J. Power Sources* **2013**, *235*, 67.
[34] L. Zhuo, Y. Wu, J. Ming, L. Wang, Y. Yu, X. Zhang, F. Zhao, *J. Mater. Chem. A* **2013**, *1*, 1141.
[35] K. S. Kim, *Phys. Rev. B* **1975**, *11*, 2177.
[36] Y. Liu, X. Zhang, *Electrochim. Acta* **2009**, *54*, 4180.
[37] G.-P. Kim, S. Park, I. Nam, J. Park, J. Yi, *J. Mater. Chem. A* **2013**, *1*, 3872.
[38] B. G. Choi, S. J. Chang, Y. B. Lee, J. S. Bae, H. J. Kim, Y. S. Huh, *Nanoscale* **2012**, *4*, 5924.
[39] A. K. Rai, J. Gim, L. T. Anh, J. Kim, *Electrochim. Acta* **2013**, *100*, 63.
[40] B. Li, H. Cao, J. Shao, G. Li, M. Qu, G. Yin, *Inorg. Chem.* **2011**, *50*, 1628.
[41] J. Jamnik, J. Maier, *Phys. Chem. Chem. Phys.* **2003**, *5*, 5215.
[42] J.-Y. Shin, D. Samuelis, J. Maier, *Adv. Funct. Mater.* **2011**, *21*, 3464.
[43] Y. Xiao, C. Hu, M. Cao, *J. Power Sources* **2014**, *247*, 49.
[44] W. Yuan, D. Xie, Z. Dong, Q. Su, J. Zhang, G. Du, B. Xu, *Mater. Lett.* **2013**, *97*, 129.
[45] J. Zhu, L. Bai, Y. Sun, X. Zhang, Q. Li, B. Cao, W. Yan, Y. Xie, *Nanoscale* **2013**, *5*, 5241.
[46] X. Yang, K. Fan, Y. Zhu, J. Shen, X. Jiang, P. Zhao, C. Li, *J. Mater. Chem.* **2012**, *22*, 17278.
[47] N. Venugopal, D.-J. Lee, Y. J. Lee, Y.-K. Sun, *J. Mater. Chem. A* **2013**, *1*, 13164.
[48] J. Sun, H. Liu, X. Chen, D. G. Evans, W. Yang, *Nanoscale* **2013**, *5*, 7564.
[49] L. Li, G. Zhou, X.-Y. Shan, S. Pei, F. Li, H.-M. Cheng, *J. Power Sources* **2014**, *255*, 52.

Manuscript received: May 7, 2015
Accepted article published: May 28, 2015
Final article published: ■■ ▮▮, 0000

FULL PAPER

Beneficial infiltration: Composites of mesoporous Co_3O_4 nanosheets (Co_3O_4-NS) and nitrogen-doped reduced graphene oxide (N-rGO) are synthesized by a facile hydrothermal approach (see figure). Excellent lithium-storage properties have been observed through a conversion mechanism.

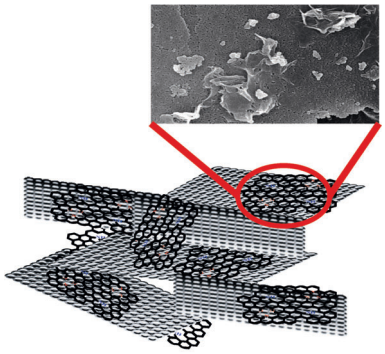

N-rGO/Co_3O_4 nanosheets composite

Electrochemistry

*Palanichamy Sennu, Hyo Sang Kim, Jae Youn An, Vanchiappan Aravindan, Yun-Sung Lee**

■■ – ■■

Synthesis of 2D/2D Structured Mesoporous Co_3O_4 Nanosheet/N-Doped Reduced Graphene Oxide Composites as a Highly Stable Negative Electrode for Lithium Battery Applications